ELSEVIER

Journal of Alloys and Compounds 456 (2008) 85–95

Journal of ALLOYS AND COMPOUNDS

www.elsevier.com/locate/jallcom

Modeling of microstructure formation of Ti–6Al–4V alloy in a cold crucible under electromagnetic field

S.P. Wu [a], D.R. Liu [b,*], Y.Q. Su [a], E.J. Guo [b], Y.H. Zhang [a]

[a] *School of Materials Science and Engineering, Harbin Institute of Technology, P.O. Box 434, Harbin 150001, China*
[b] *School of Materials Science and Engineering, Harbin University of Science and Technology, No. 4 Lin Yuan Road, Dong Li District, Harbin 150040, China*

Received 16 November 2006; received in revised form 1 February 2007; accepted 1 February 2007
Available online 6 February 2007

Abstract

An integrated macro/micro model is developed for simulating the microstructure evolution during solidification processes of Ti–6Al–4V alloy in a cold crucible under electromagnetic field, which combines the 3-D finite difference method (FDM) at the macroscale with a 2-D cellular automaton (CA) model at the microscale. Based on the FDM solution of momentum, thermal transport and Maxwell equations, the macro model is used to simulate the fluid flow and heat transfer throughout the casting under electromagnetic field. The micro model is used to predict the nucleation and growth of grains for the vertical central plane. Validity of the model is confirmed by comparison between the result from calculation and it from direct measurement. Numerical simulations are performed to investigate the influences of coil current, duration and heat transfer coefficient at the casting/crucible interface on fluid flow and microstructure formation. Calculated results reveal that the growth of coarser columnar structure is promoted for a longer duration. The variation of coil current has a minor effect on the formation of microstructure. Increasing the heat transfer coefficient generates a coarser cast structure. The main action of electromagnetic field is that a small vortex in the upper part rotates in opposite direction to the buoyancy convection. The underlying mechanisms responsible for those physical phenomena are discussed.

Keywords: Modeling; Microstructure formation; Ti–6Al–4V alloy; Electromagnetic field; Cold crucible

1. Introduction

It is well known that titanium and its alloys may be used as hydrogen storage media because of their high affinity on hydrogen. It was not until recently that hydrogen, when used correctly, can be recognized as a beneficial element because of its influences on the modification of microstructures, such as microstructure refinement, and the consequent enhancement of mechanical properties [1]. Therefore, thermohydrogen processing with hydrogen acting as a temporary element has attracted a great deal of interest for refining the microstructure of titanium alloys. And the best known alloy, which has been widely used and studied, is Ti–6Al–4V [1,2].

As numerous experimental investigations on thermohydrogen processing to Ti–6Al–4V alloy have been published [3,4], it can be found that if the hydride TiH_2 is used as the source of hydrogen, the hydrogenation process usually is executed in the cold crucible under electromagnetic field, since this technique offers many varieties of application such as melting and casting of active metals with high melting points. Therefore, before the underlying mechanisms of microstructure refinement by hydrogen treatment are explored, grain structure solidified in the cold crucible under electromagnetic field should be studied first.

Although experimental studies can be carried out to investigate possible mechanisms for microstructure formation, it is still difficult to use those experiments to explain the results in the real castings, because of the opaqueness of the alloy melt. However, the numerical methods, such as deterministic and cellular automaton (CA) models [5], offer the possibility to "visualize" all the details.

For the prediction of microstructure formation, deterministic models have been first proposed. However, the structural features such as grain morphology and size cannot be depicted graphically by them [6]. Therefore, the stochastic method, such as CA

* Corresponding author. Tel.: +86 451 86418815.
E-mail address: hlgldr@126.com (D.R. Liu).

0925-8388/$ – see front matter © 2007 Elsevier B.V. All rights reserved.
doi:10.1016/j.jallcom.2007.02.006

Nomenclature

$\overline{B}$ magnetic flux density
B_r radial component of $\overline{B}$
B_x, B_y, B_z components of $\overline{B}$ in X, Y and Z direction, respectively
c_p specific heat
C_o initial alloy composition
D_l liquid diffusion coefficient
f_l, f_s volume fraction
$\overline{F}$ Lorentz force
F_x, F_y, F_z components of Lorentz force in X, Y and Z direction, respectively
g gravitational acceleration
$\mathrm{hi}_{max}, \mathrm{hi}_{min}$ heat transfer coefficient at the casting/crucible interface
H_c height of the coil
I coil current
$\overline{J_e}$ electric current density
J_{ex}, J_{ey}, J_{ez} x, y and z components of $\overline{J_e}$
k partition coefficient of phase diagram
K permeability of liquid in porous medium
L volumetric latent heat
m liquidus slope of phase diagram
n nuclei density
n_{max} maximum nuclei density
N number of coil turns
P pressure
$Q_{induction}$ joule heat per unit volume
r_{cell} growth length of dendrite tip
r_o radius of the coil
r_p distance of a point to the z-axis
t time
T temperature
T_p pouring temperature
T_{ref} reference temperature
ΔT undercooling
ΔT_c constitutional undercooling
ΔT_{max} mean nucleation undercooling of the Gaussian distribution
ΔT_σ standard deviation of the Gaussian distribution
u, v and w X, Y and Z components of $\overline{U}$
$\overline{U}$ velocity vector
$V_{tip}(\Delta T_c)$ growth velocity of dendrite tip
Δx_{cell} cell size
Δx_{FDM} size of finite difference mesh
z_o half height of the coil
z_p distance of a point to the central x–y plane

Greek symbols
β_T thermal expansion coefficient
Γ Gibbs-Thomson coefficient
ε magnetic permeability
θ angle between radial magnetic flux density and x-axis
λ thermal conductivity
μ viscosity
ρ density
σ electrical conductivity

technique, is introduced to simulate the microstructure evolution during the course of solidification. Although great efforts and progress have been made to model microstructure evolution with CA models over the last decade [5–9], we can find:

(1) The microstructure formation and electromagnetically driven flow in the cold crucible have been studied as separate subjects in many literatures. However, it is useful to note that until now there has not been an integrated computational methodology to quantify the effects of electromagnetically induced flow on microstructure in the cold crucible. Furthermore, investigation of solidification behavior under electromagnetic field is of prime importance as this may provide the framework for further study of hydrogenation characteristics and the microstructure modification of Ti–6Al–4V by hydrogen treatment.
(2) It is well known that operation parameters, such as coil current, duration and heat transfer coefficient at the casting/crucible interface, have significant effects on the microstructure formation during solidification. However, there are few studies about the influences of these parameters. And the parametric study is very necessary for our fundamental understanding of fluid flow and microstructure evolution under electromagnetically assisted condition in a cold crucible.

Therefore, in the present study, an integrated macro/micro model is presented which is based on the coupling of the 3-D FDM method for macroscopic modeling of fluid flow and heat transfer phenomena and the 2-D CA model for simulating microstructure evolution of Ti–6Al–4V in the cold crucible. An important relationship between the melt temperature and the coil current is constructed based on the experimentally measured cooling curve. This model is verified by comparing the numerical prediction with experimental observation. Effects of operation parameters, such as coil current, duration and heat transfer coefficient on the fluid flow and microstructure evolution are investigated in detail.

2. Macroscopic model

Simulation of the solidification of Ti–6Al–4V alloy in the cold crucible under electromagnetic field is considered in a three-dimensional domain and modeled by solving the governing equations of continuity and momentum for fluid flow, the thermal balance equation for heat transfer and the Maxwell equation for electrodynamics. In derivation of these equations, the following simplifying assumptions are made.

(1) No interaction for the coupling between the electromagnetic field and the melt shape is considered. The shape of the molten alloy is simply input to match the experimental result.
(2) Nucleation sites are stationary and do not move with the melt.
(3) All thermophysical properties are assumed to be constant.

Based on these hypotheses, the continuity and momentum equations (Cartesian coordinate system) for the steady and incompressible thermal flow are given as [10,11]:

$$\nabla(\rho\overline{U}) = 0 \tag{1}$$

$$\rho\frac{\partial u}{\partial t} + \rho\nabla(u\overline{U}) = -\frac{\partial P}{\partial x} + \nabla(\mu\nabla u) + \frac{\mu}{K}u + F_x \tag{2}$$

$$\rho\frac{\partial v}{\partial t} + \rho\nabla(v\overline{U}) = -\frac{\partial P}{\partial y} + \nabla(\mu\nabla v) + \frac{\mu}{K}v + F_y \tag{3}$$

$$\rho\frac{\partial w}{\partial t} + \rho\nabla(w\overline{U}) = -\frac{\partial P}{\partial z} + \nabla(\mu\nabla w) + \frac{\mu}{K}w - \rho g[\beta_{\mathrm{T}}(T - T_{\mathrm{ref}})] + F_z \tag{4}$$

The last terms in the right hand side of Eqs. (2)–(4) are components of Lorentz force $\overline{F}$ in X, Y and Z directions, respectively.

$$F_x = J_{\mathrm{e}y}B_z - J_{\mathrm{e}z}B_y \tag{5}$$

$$F_y = J_{\mathrm{e}z}B_x - J_{\mathrm{e}x}B_z \tag{6}$$

$$F_z = J_{\mathrm{e}x}B_y - J_{\mathrm{e}y}B_x \tag{7}$$

The current density $\overline{J_{\mathrm{e}}}(J_{\mathrm{e}x}, J_{\mathrm{e}y}, J_{\mathrm{e}z})$ is generated by the induced electric field and the movement of materials under the externally imposed magnetic field and can be calculated by solving the Maxwell equation [11]:

$$\overline{J_{\mathrm{e}}} = \sigma\left[-\left(\frac{\Delta x_{\mathrm{FDM}}}{2}\right)\nabla(\overline{U}\times\overline{B}) + \overline{U}\times\overline{B}\right] \tag{8}$$

For some solidification problem, in order to simplify the method and allow reasonable computation time, in this paper, components of the magnetic flux density $\overline{B}$ in different directions are calculated by semi-empirical equations [12]:

$$B_z = \frac{N}{H_{\mathrm{c}}}\int_{-z_{\mathrm{o}}}^{z_{\mathrm{o}}}\frac{\varepsilon I}{2\pi z_{\mathrm{o}}}\frac{1}{\sqrt{(r_{\mathrm{o}}+r_{\mathrm{p}})^2+(z_{\mathrm{p}}-z)^2}} \times \left|1.46\times\frac{r_{\mathrm{p}}^2-r_{\mathrm{o}}^2-(z_{\mathrm{p}}-z)^2}{(r_{\mathrm{p}}-r_{\mathrm{o}})^2+(z_{\mathrm{p}}-z)^2}+1.677\right|\mathrm{d}z \tag{9}$$

$$B_{\mathrm{r}} = \frac{N}{H_{\mathrm{c}}}\int_{-r_{\mathrm{o}}}^{r_{\mathrm{o}}}\frac{\varepsilon I}{2\pi r_{\mathrm{p}}}\frac{(z_{\mathrm{p}}-z_{\mathrm{o}})}{\sqrt{(r_{\mathrm{p}}+r)^2+(z_{\mathrm{p}}-z_{\mathrm{o}})^2}} \times \left|1.46\times\frac{r^2+r_{\mathrm{p}}^2+(z_{\mathrm{p}}-z_{\mathrm{o}})^2}{(r_{\mathrm{p}}-r)^2+(z_{\mathrm{p}}-z_{\mathrm{o}})^2}+1.677\right|\mathrm{d}r \tag{10}$$

$$B_x = B_{\mathrm{r}} \times \cos\theta \tag{11}$$

$$B_y = B_{\mathrm{r}} \times \sin\theta \tag{12}$$

Heat transfer model is [12]:

$$\frac{\partial T}{\partial t} + \nabla(T\overline{U}) = \frac{\lambda}{\rho c_{\mathrm{p}}}\nabla(\nabla T) + \frac{L}{c_{\mathrm{p}}}\frac{\partial f_{\mathrm{s}}}{\partial t} + \frac{Q_{\mathrm{induction}}}{\rho c_{\mathrm{p}}} \tag{13}$$

where $Q_{\mathrm{induction}}$ is joule heat per unit volume. Details about its calculation are given in Ref. [12].

In the Cartesian coordinate, a FDM formulation is chosen to solve these equations. The calculation procedure is the following. First of all, the distributions of magnetic flux density for each coil current are estimated by Eqs. (9)–(12). Secondly, momentum and continuity equations are solved by the solution algorithm volume of fluid (SOLA-VOF) technique. Thirdly, based on the distributions of the magnetic field and the flow field, the current density can be calculated by Eq. (8). Finally, Lorentz force induced by the magnetic field is determined by solving Eqs. (5)–(7). This procedure is repeated within each time-step.

Here one point should be stressed. As the severity of segregation is dependent on the partition coefficient of the element, there is little segregation of aluminum ($k_{\mathrm{Al}} = 1.167$) and vanadium ($k_{\mathrm{V}} = 0.84$). It indicates that during the solidification of Ti–6Al–4V alloy, the solutal convection, induced by the concentration gradient due to the rejection of solute into the interdendritic liquid, may not play a significant role. Thus, the solutal buoyancy term is not considered in the momentum equation.

3. Microscopic model

For the simulation of grain nucleation and growth, a microscopic model has been developed by Rappaz et al. [6], characterized as the thermal undercooling and a power law can be reasonably used for the calculations of nucleation and growth, respectively. In this study, their idea has been adopted without any modifications.

3.1. Nucleation model

A Gaussian distribution is given:

$$\frac{\mathrm{d}n}{\mathrm{d}(\Delta T)} = \frac{n_{\max}}{\sqrt{2\pi}\Delta T_\sigma}\exp\left[-\frac{(\Delta T-\Delta T_{\max})^2}{2\Delta T_\sigma^2}\right] \tag{14}$$

3.2. Growth model

Once nucleation has occurred, a rule for tip growth must be applied. Here, the $V_{\mathrm{tip}}(\Delta T_{\mathrm{c}})$ relationship is described by a power law, which fits the KGT (Kurz–Giovanola–Trivedi) model [13]:

$$V_{\mathrm{tip}}(\Delta T_{\mathrm{c}}) = 5.85\times10^{-6}(\Delta T_{\mathrm{c}})^2 \tag{15}$$

Then, the growth length of the dendrite tip is given by:

$$r_{\mathrm{cell}}(t) = \int_0^t V_{\mathrm{tip}}[\Delta T_{\mathrm{c}}(t^*)]\,\mathrm{d}t^* \tag{16}$$

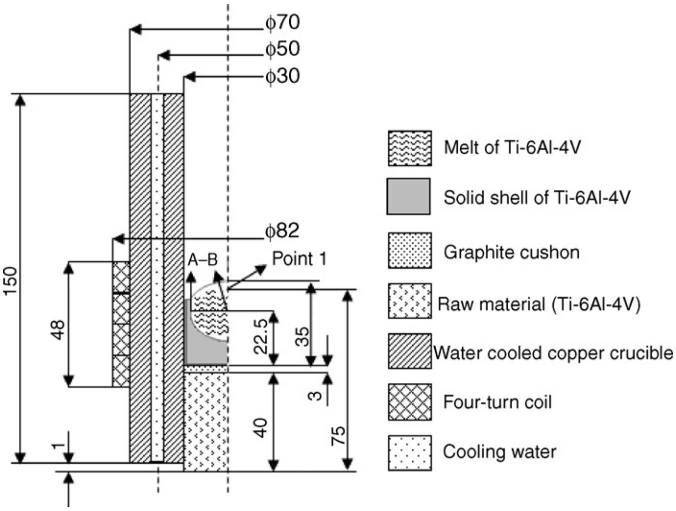

Fig. 1. Schematic diagram of the cold crucible.

4. Experimental technique

The schematic representation of the whole geometry of cold crucible is shown in Fig. 1, where all dimensions are in millimeters. The cold crucible is made of copper with 30 mm in internal diameter, 70 mm in external diameter, and 150 mm in height and a four-turn water cooled copper coil with 12 mm in diameter is located around it. This cylindrically straight crucible has eight pieces of vertical slits periodically arranged along the circumferential direction.

For a typical cold crucible casting procedure, the cylindrical Ti–6Al–4V charge with 30 mm in diameter is first placed at a certain position in the crucible where the influence of an induction coil is active. Then the furnace chamber is filled with argon with slight overpressure compared to atmospheric pressure. The power is gradually increased until the charge melts with the formation of a meniscus. After holding the melt for a period of time, as the steady state is reached, the power is decreased at a certain rate. When the melt has completely solidified, the pressure is released and the crucible arrangement taken down to remove the casting.

5. Relationship between the temperature and the coil current

From the above description, we can see that, at the first step, the alloy is heated and melted due to the transmission of the power until a certain superheat is achieved. As the calculation of the heating process of Ti–6Al–4V alloy is not included in this paper, for the following simulation, a reasonable approximation should be given to estimate the melt temperature at the beginning of solidification. Therefore, an attempt is made to provide a relationship between the temperature and the coil current. For that purpose, by varying the coil current, temperature measurement was made within the melt during solidification using one W–3Re/W–25Re thermocouple that was installed along the casting axis at the fixed vertical position of 75 mm measured from the base of the raw material (point 1, see Fig. 1).

As shown in Fig. 2, the relationship between the temperature and the coil current is constructed on the basis of the experimentally measured cooling curve (Fig. 2(a)) through the use of regression-correlation analysis:

$$T_{\mathrm{p}} = -0.00045 \times I^2 + 1.77448 \times I - 103.2 \qquad (17)$$

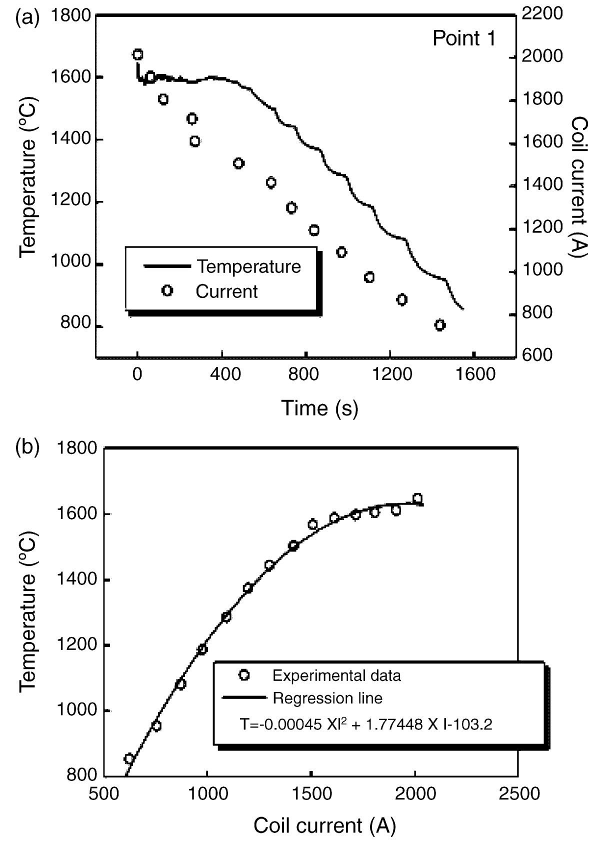

Fig. 2. Relationship between the measured temperature and the coil current: (a) experimental data; (b) regression correlation.

Here one point should be stressed that although this relationship can only be applied to point 1 in theory, to circumvent the lack of the complete analysis of heating process, for the following calculation, it is assumed that at the beginning of solidification, the whole melt has a uniform temperature, which can be specified using Eq. (17). While this assumption may not be strictly correct, it is the best approximation available at this time.

6. Results and discussion

The present mathematical model is applied to simulate the microstructure evolution during solidification of Ti–6Al–4V

Table 1
Thermo-physical data used in the simulation

	Ti–6Al–4V	Copper
λ ($\mathrm{Wm^{-1}\,K^{-1}}$)	14.1	398
c_{p} ($\mathrm{Jkg^{-1}\,K^{-1}}$)	930	465
ρ ($\mathrm{kg\,m^{-3}}$)	4430	8930
L ($\mathrm{Jm^{-3}}$)	1580×10^6	
$T_{\mathrm{l}}/T_{\mathrm{ref}}$ (°C)	1635	
T_{s} (°C)	1522	
T_{m} (°C)	1670	
μ ($\mathrm{m^2\,s^{-1}}$)	4×10^{-5}	
β_{T} ($\mathrm{K^{-1}}$)	2×10^{-4}	
σ ($\mathrm{MSm^{-1}}$)	0.688	
ε ($\mathrm{Hm^{-1}}$)	12.6×10^{-7}	

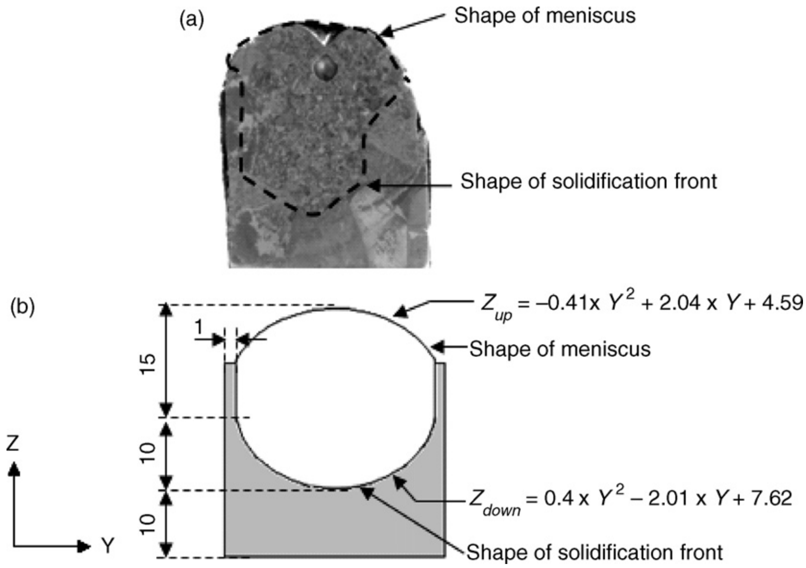

Fig. 3. Shape of the molten melt: (a) experimental result and (b) shape functions for numerical calculation.

Table 2
Parameters used in the simulation

Properties	Value
D_l ($m^2\,s^{-1}$)	5×10^{-9}
n_{max} (m^{-3})	3×10^{9}
ΔT_σ (°C)	0.5
ΔT_{max} (°C)	1
Δx_{cell} (m)	1×10^{-4}
Δx_{FDM} (m)	1×10^{-3}

alloy under the electromagnetic field in the cold crucible. The physical properties of Ti–6Al–4V and copper crucible are included in Table 1 [14]. Other parameters used for simulation are listed in Table 2. Boundary types and heat transfer coefficients are given in Table 3 [15]. Here, the value of hi_{max} is assumed constant 1000 W/(m^2K) and four different values of hi_{min}, 20, 100, 400 and 800 W/(m^2K), are selected to investigate

Table 3
Boundary types and heat transfer coefficients

	Expression
Metal top and argon gas (type A)	$Q_A = h_{rA}(T_{gas} - T_{metal})$ $h_{rA} = 1.05 \times \xi \times [(T_{gas} + 273)^2 + (T_{metal} + 273)^2][(T_{gas} + 273) + (T_{metal} + 273)]$
Metal and solid shell (type B)	$Q_B = \lambda_{metal}(T_{shell} - T_{metal})$
Solid shell and crucible interface (type C)	$Q_C = h_{rC}(T_{crucible} - T_{metal})$ $h_{rC} = h_{conduction} + (1 - f_l)h_{radiation}$ $h_{conduction} = hi_{min} + f_l(hi_{max} - hi_{min})$ $h_{radiation} = 0.4 \times \xi \times [(T_{crucible} + 273)^2 + (T_{metal} + 273)^2][(T_{crucible} + 273) + (T_{metal} + 273)]$ $\xi = 0.72 \quad hi_{max} = 1000\,Wm^{-2}\,K^{-1}$

the influence of the rate of heat extraction on the evolution of microstructure.

6.1. Validation of the present model

To evaluate the validity of the proposed model, the numerical prediction is compared with the experimental measurement. To correspond to the production conditions, the mathematical modeling is performed with the coil current 2015 A and duration 300 s meaning that the coil current is kept constant during this period of time and soon decreased to zero as solidification progresses. The heat transfer coefficient hi_{min} is taken as 20 W/(m^2K).

As the shape of the molten Ti–6Al–4V alloy in the cold crucible is assumed constant during solidification, the experimentally obtained morphologies of solidification front and meniscus (indicated as dashed lines, Fig. 3(a)) are input to the model. The corresponding shape functions are presented in Fig. 3(b).

The validation of the present model investigates the microstructure of Ti–6Al–4V alloy. Fig. 4 gives the comparison of experimentally observed and numerically predicted microstructures. It can be seen that the simulation is in reasonable agreement with the experimental observation, although

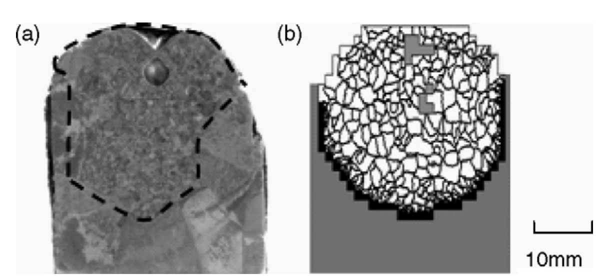

Fig. 4. Comparison between: (a) experimentally observed and (b) numerically predicted microstructure.

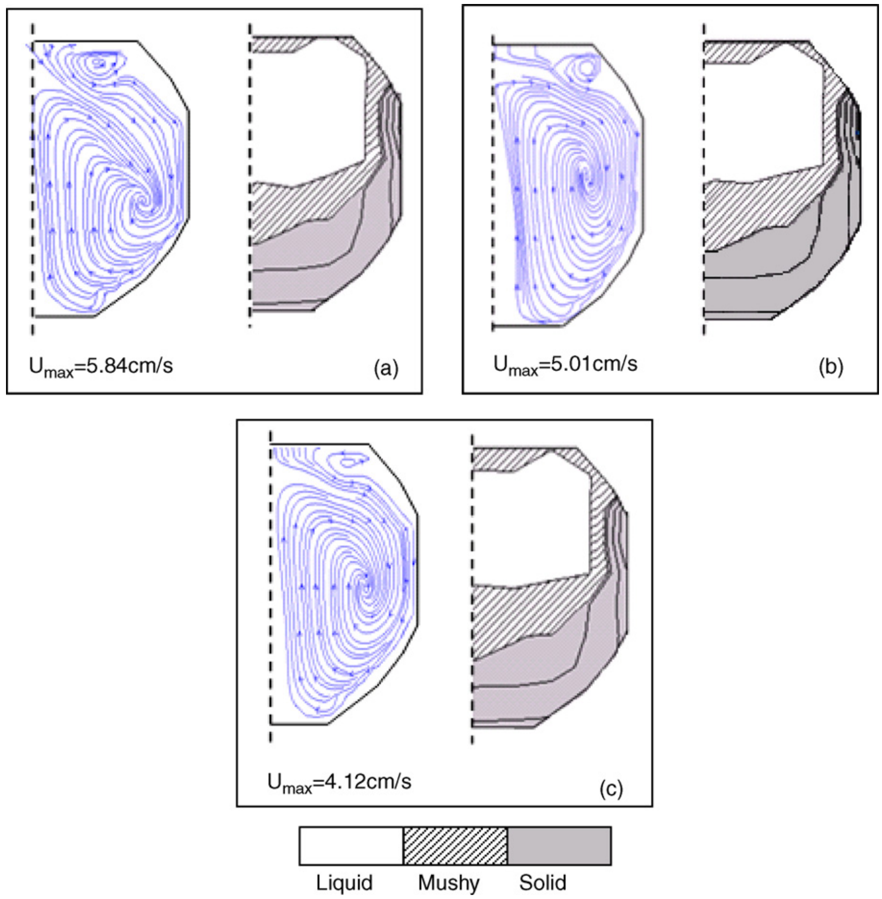

Fig. 5. Calculated streamline and the extent of mushy zone at 5 s for: (a) 2015 A; (b) 1893 A and (c) 1862 A.

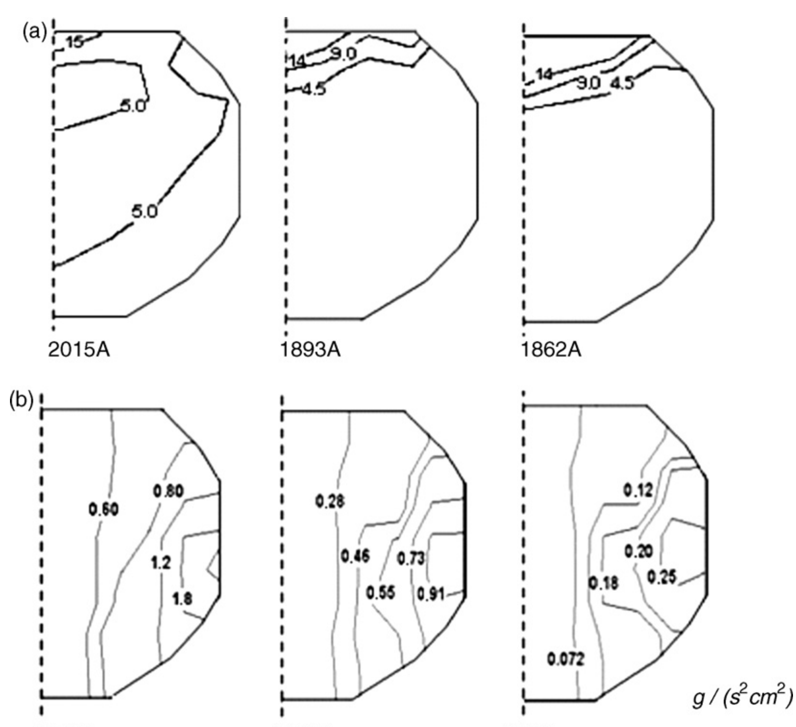

Fig. 6. Distributions of buoyancy and Lorentz forces for various coil currents at 5 s: (a) buoyancy force and (b) Lorentz force.

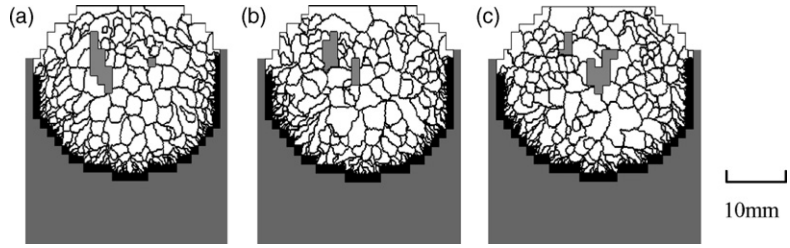

Fig. 7. Simulated microstructures of Ti–6Al–4V alloy for various coil currents with hi_{min} 20 W/(m^2K): (a) 2015 A; (b) 1893 A and (c) 1862 A.

there is an over-prediction of the mean grain size. Notwithstanding this discrepancy, the validity of the developed model can still be confirmed.

6.2. *Effect of coil current*

To investigate the effect of coil current, we perform numerical simulations by selecting three currents: 2015, 1893 and 1862 A. And for each coil current, the duration is 5 s, after which the coil current is soon decreased to zero.

Fig. 5 compares the streamline and the size of mushy zone at solidification time 5 s for various coil currents. As we know, convection can be the result of two body forces within the bulk liquid. First, convection can be created by gravity associated with a temperature gradient. Second, external force such as electromagnetic force (Lorentz force) can also induce significant fluid flow. Since the electromagnetically driven flow may counteract the basic buoyancy flow in the melt, in view of Fig. 5, it is observed that the molten metal in the melt pool flows in two cells. The first one, basic buoyant flow, is characterized by a downward melt flow along the vertical crucible wall and a corresponding upward flow in the middle of the casting. The second one caused by Lorentz force, opposite to the thermal convection, flows from the meniscus top down and returns through the free melt surface. In addition, it can be found that the size of second cell located in the upper part of the melt is usually small, which can be explained by the competing effects of the two body forces. Fig. 6 gives the distributions of buoyancy and Lorentz forces for various coil currents at 5 s. As the Lorentz force ($\sqrt{F_y^2 + F_z^2}$) is not sufficiently large compared with the buoyancy force ($\rho g[\beta_T(T - T_{ref})]$), the effects of thermal buoyancy outweigh the effects of electromagnetic force, suppressing the formation of a large counter-clockwise rotating flow in the upper part of the melt.

Although the overall flow patterns appear in the three cases similarly, there is a change in the magnitude of the maximum flow velocity. The strength of fluid flow is increased as a larger coil current is selected. This can be explained from two aspects. Firstly, as the coil current I and the Lorentz force $\overline{F}$ are indirectly related through the magnetic flux density $\overline{B}$, an increase in I results in the increase in $\overline{B}$ indicating an increase of $\overline{F}$, and therefore, the fluid flow in the bulk liquid is reinforced. Secondly, increasing the coil current is equalized to increasing the melt superheat (by means of Eq. (17), superheats are found to be 13, 8 and 5 °C for coil currents of 2015, 1893 and 1862 A, respectively), which may produce a stronger thermal convection in the liquid pool.

However, it is worth noting that decreasing the coil current from 2015 to 1862 A does not affect the size of mushy zone greatly. As the temperature distribution has a direct influence on the formation of microstructure in solidifying melts, it can be predicted that the obtained microstructure may not be significantly affected by changing the coil current. This can be confirmed by examination of the following two figures.

Figs. 7 and 8 show the predicted microstructures of Ti–6Al–4V alloy and the mean grain sizes obtained for different coil currents, respectively. A prominent feature is the fact that the simulated microstructure is nearly independent of the coil current. This is somewhat surprising when one considers that increasing the coil current serves to increase the melt initial temperature. Thus, one might expect the coarser microstructure is formed with a larger superheat. Since increasing the coil current may increase the strength of fluid flow, which may overcome the higher thermal load imposed by the higher superheat, nullifying the effect of superheat, it is not surprising to see that the microstructure is little affected.

6.3. *Effect of duration*

In order to quantify the effects of duration on microstructure formation, four cases have been designed presenting the different combinations of coil current and duration, as shown in Fig. 9.

Figs. 10 and 11 show the evolutions of microstructure at various solidification times and the mean grain sizes for different

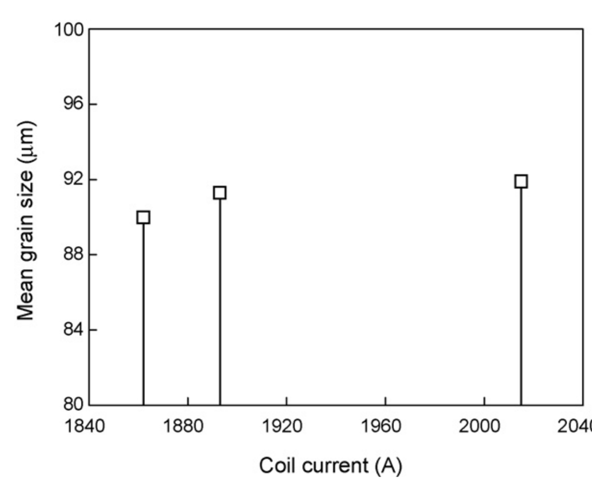

Fig. 8. Dependence of mean grain size on the coil current.

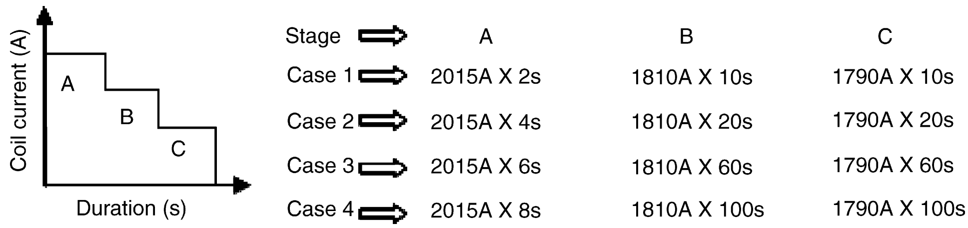

Fig. 9. Different combinations of the coil current and duration.

cases, respectively. In view of the results, it is clear that the growth of coarser columnar grain is promoted with increasing the duration. For the explanation, efforts have gone into understanding the competition between the growth of columnar and equiaxed grains.

Firstly, during stage A, the columnar grain grows slowly and no nucleation of equiaxed grain occurs. This is mainly attributed to the fact that as the initial superheat (13 °C) is not fully dissipated, the remaining superheat leads to a significant delay of the microstructure formation. And the degree of the postponement of solidification increases with increasing the duration. Secondly, during stage B, with decreasing the coil current from 2015 to 1810 A, constitutional undercooling ($T_p - T_L = 1\,°C$, Eq. (17)) is soon built up in the melt and its intensity is suf-

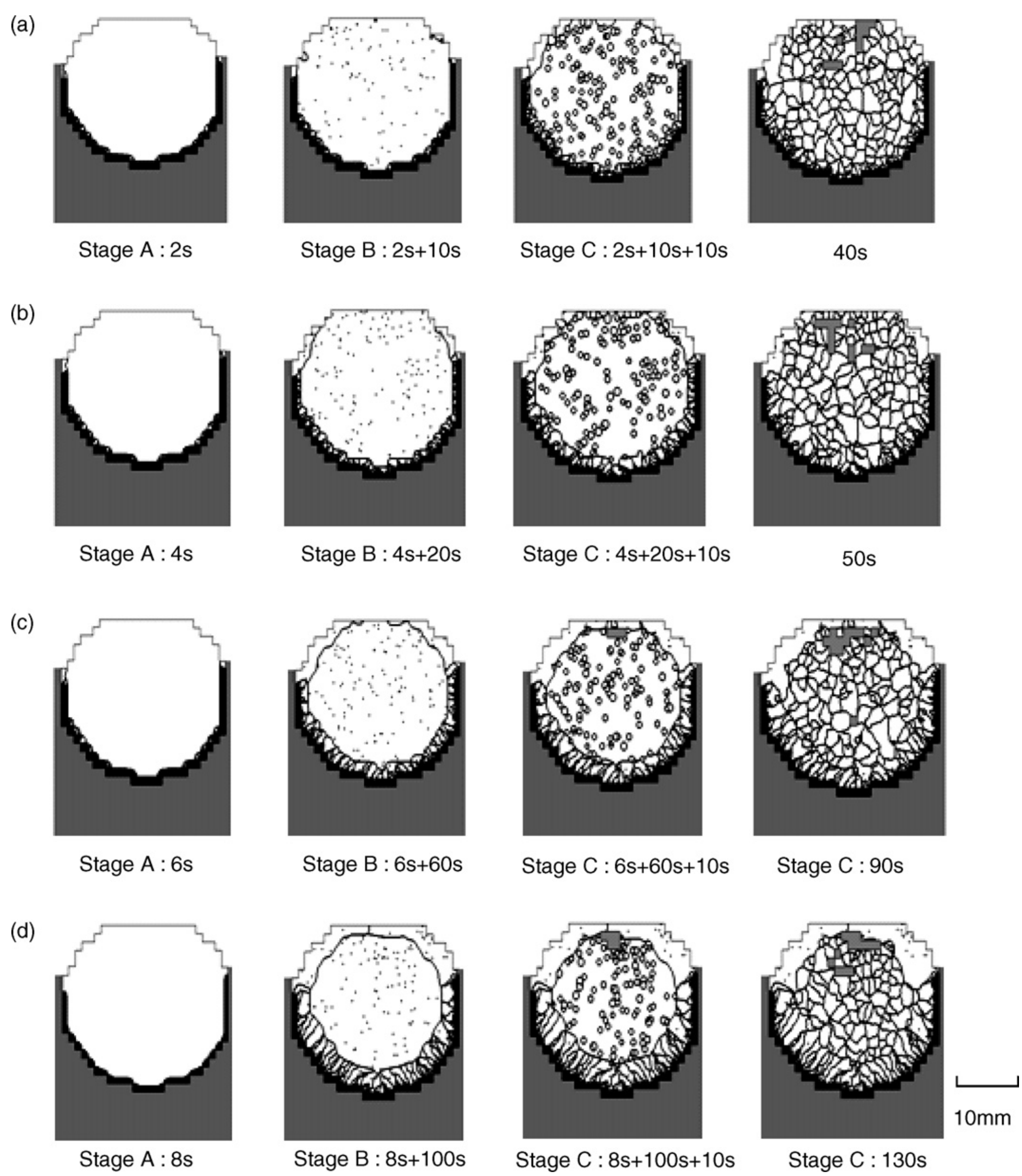

Fig. 10. Simulated microstructures of Ti–6Al–4V alloy at various solidification times for different cases with hi_{min} 20 W/(m^{2}K): (a) case 1; (b) case 2; (c) case 3 and (d) case 4.

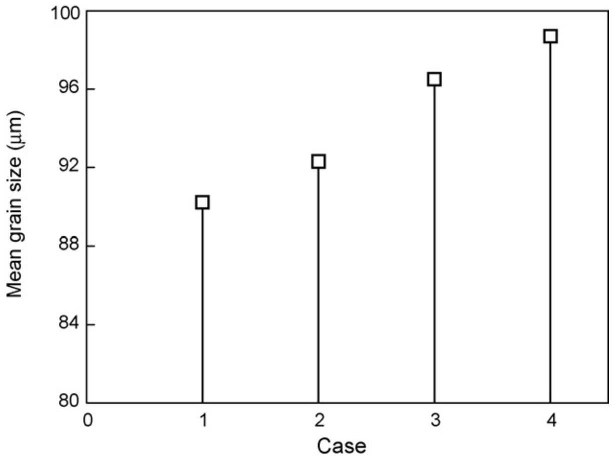

Fig. 11. Variation of mean grain size for different cases.

ficient to allow the nucleation of equiaxed grains over a short period of time due to a small nucleation undercooling selected ($\Delta T_{max} = 1\,^{\circ}C$, see Table 2). Despite the fact that an amount of nuclei are present in the melt during this stage, the constitutional undercooling is still too low to allow equiaxed growth. Thus, since a larger temperature gradient exists ahead of the columnar front due to the heat loss at the edge of the casting, only columnar growth is possible and the increase of its length runs parallel to the increase of duration. Thirdly, during stage C, with further decreasing the coil current from 1810 to 1790 A, the average liquid temperature decreases, corresponding to a lower value. At this time the undercooled region widens and constitutional undercooling (4 °C) increases, and then, the equiaxed grains may develop from the nuclei present in the melt. Their growth soon hinders the columnar growth building the central equiaxed zone. It can be found that during this stage, for cases 3 and 4, the time required for the complete microstructure formation is shorter compared to the pre-determined duration. That is to say, further increase in duration beyond the value of 24 s may not have apparent influence on the microstructure formation.

It becomes obvious that the duration plays a significant role in the course of solidification, especially during stages A and B. In fact, the generation of joule heat is responsible for this phenomenon. The contour lines of joule heat generated during the casting process are shown in Fig. 12. The larger the coil current, the more the joule heat generated. It is also expected that more joule heat is produced during solidification for the longer duration. As the joule heat can be considered as the resistance for the heat transfer from the casting to the crucible, the cooling rate during solidification is inversely proportional to the amount of generated joule heat and the length of duration. Thus, different durations find expression in the fineness of the structure: with a longer duration, the microstructure becomes coarser.

6.4. *Effect of heat transfer coefficient*

To characterize the heat transfer coefficient hi_{min} effect, we perform numerical simulations by selecting four hi_{min}: 20, 100, 400 and 800 W/(m^{2}K). With the same coil current 2015 A and duration 5 s, Figs. 13 and 14 present the predicted microstructures of Ti–6Al–4V alloy for different hi_{min} and the corresponding mean grain sizes, respectively. From the data shown in the above two pictures, the following information can be extracted: a coarser microstructure is easily formed for the case of a larger heat transfer coefficient. This is mainly attributed to the fact that as the rate of heat extraction to the crucible is higher with a larger hi_{min}, the temperature gradient increases in the casting, which reduces the size of the undercooled region,

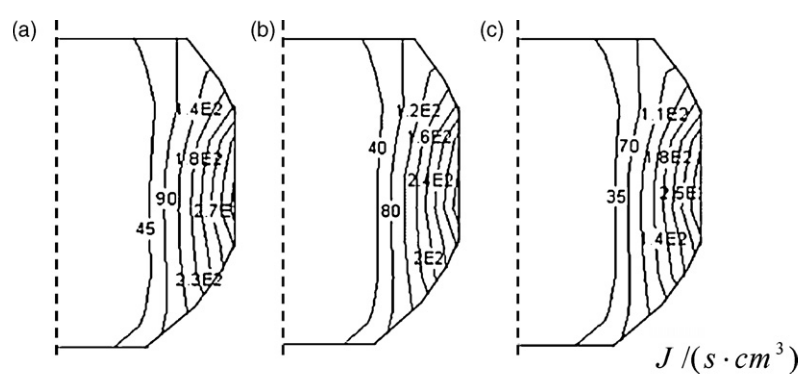

Fig. 12. Contour lines of joule heat generated for various coil currents: (a) 2015 A; (b) 1810 A and (c) 1790 A.

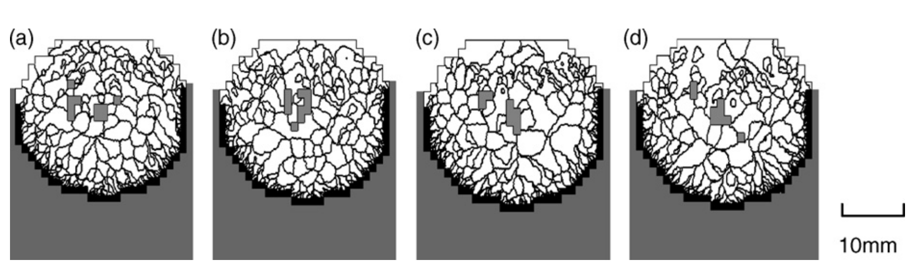

Fig. 13. Simulated microstructures of Ti–6Al–4V alloy for various heat transfer coefficients (W/m^{2}K): (a) 20; (b) 100; (c) 400 and (d) 800.

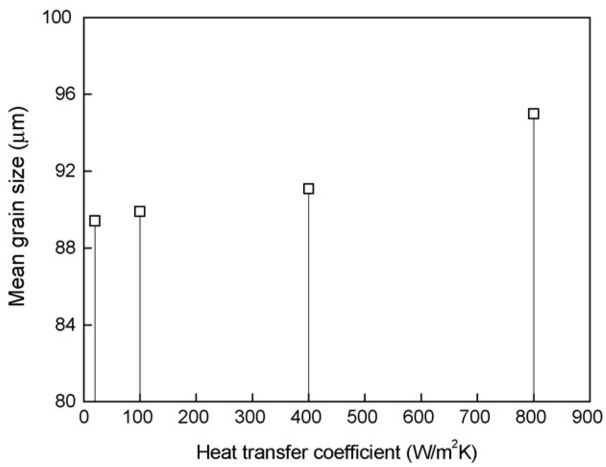

Fig. 14. Dependence of mean grain size on the heat transfer coefficient.

and then reducing the probability of sufficient nucleation of equiaxed grains. Therefore, the development of the coarser columnar region is favored at the expense of the finer equiaxed zone, generating a coarser cast structure.

This phenomenon can be further explained by studying the thermal profiles within the casting (from point A to B, see Fig. 1) during solidification. As shown in Fig. 15, the establishment of a

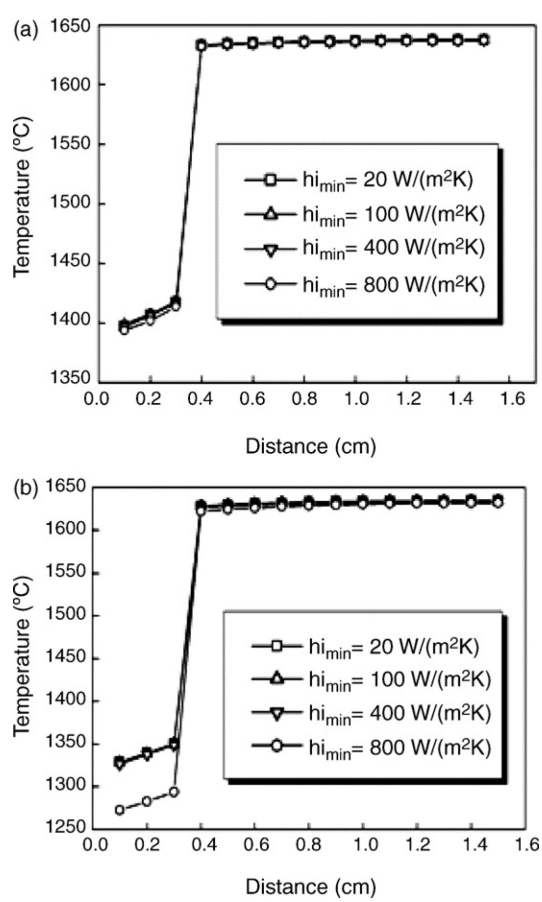

Fig. 15. Temperature distribution profiles in the casting (from point A to B, see Fig. 1) calculated for various heat transfer coefficients at different times. On the *x*-axis, zero represents the interface between the casting and the crucible: (a) 5 s and (b) 10 s.

steeper temperature gradient is encouraged by increasing hi_{min}, which may induce a higher cooling rate meaning that there is less time for equiaxed grains to nucleate and grow. Consequently, as the coarser columnar growth is promoted, the mean grain size increases with the heat transfer coefficient.

As the heat transfer coefficient is a parameter which is dependent on the existing conditions, such as interfacial conditions, properties of both casting material and mould material, processing variables, varying the heat transfer coefficient should be linked with all the above factors: it is not possible to alter the heat transfer coefficient independently in the real process. However, the model in the present study assumes that the heat transfer coefficient and other parameters are decoupled, since an “ideal” model incorporating all physical phenomena in a fully coupled manner may be complex and not be industrially viable. Despite this limitation, the simulation still provides useful insight into the sensitivity of the microstructure to variations in the heat transfer coefficient.

7. Conclusions

An integrated macro/micro model has been developed for simulating microstructure formation of Ti–6Al–4V alloy in the cold crucible under electromagnetic field. The mathematical formulations consist of the continuity and momentum equations for fluid flow, the thermal balance equation for heat transfer and the Maxwell equations for electrodynamics, in combination with the CA representation of the evolution of microstructure.

Effects of operation parameters, such as coil current, duration and heat transfer coefficient, on the fluid flow and microstructure evolution of Ti–6Al–4V alloy are studied. Some characteristics can be summarized as follows:

(1) Two kinds of recirculation flow exist in the melt. They make a collision slightly in the upper part of the casting. With buoyancy force overwhelming the electromagnetic force, the vortex induced by Lorentz force is small.
(2) With a longer duration, the characteristic feature of the microstructure is the appearance of coarser columnar grain in the casting. However, varying the coil current has a minor influence on the microstructure formation. Mean grain size is highly dependent on the duration and less dependent on the coil current.
(3) The coarser columnar solidification is more likely to occur with a higher value of heat transfer coefficient that is a dominating factor in determining the grain size.

The validation with the experimental measurement generates some confidence that the present numerical model enables the reasonable predictions of fluid flow, heat transfer and microstructure formation in the cold crucible under electromagnetic field. Therefore, the model is a suggestion or guideline to the future research in microstructural modification during the hydrogenation process.

Acknowledgements

Authors would like to thank the National Science Foundation of China (No. 5039512) and Project 973 (No. 51319) for financial support.

References

[1] T.Y. Fang, W.H. Wang, Mater. Chem. Phys. 56 (1998) 35–47.
[2] A.L. Suarez, J. Rickards, R.T. Luna, Int. J. Hydrogen Energy 28 (2003) 1107–1113.
[3] O.N. Senkov, F.H. Froes, Int. J. Hydrogen Energy 24 (1999) 565–576.
[4] F.H. Froes, O.N. Senkov, J.I. Qazi, Int. Mater. Rev. 49 (2004) 227–245.
[5] Ch.A. Gandin, Ch. Charbon, M. Rappaz, ISIJ Int. 35 (1995) 651–657.
[6] M. Rappaz, Ch.A. Gandin, Acta Metall. 41 (1993) 345–360.
[7] Ch.A. Gandin, J.L. Desbiolles, M. Rappaz, Ph. Thevoz, Metall. Trans. A. 30 (1999) 3153–3165.
[8] Ch.A. Gandin, T. Jalanti, M. Rappaz, in: B.G. Thomas, C. Beckermann (Eds.), Modeling of Casting, Welding and Advanced Solidification Processes VIII, 1998, pp. 363–374.
[9] I.S. Cho, C.P. Hong, ISIJ Int. 37 (1997) 1098–1106.
[10] V. Galindo, G. Gerbeth, W.V. Ammon, E. Tomzig, J. Virbulis, Energy Convers. Manage. 43 (2002) 309–316.
[11] M.Y. Ha, H.G. Lee, S.H. Seong, J. Mater. Process. Technol. 133 (2003) 322–339.
[12] R.R. Chen, Dissertation for the Ph.D. degree of Harbin Institute of Technology, 2005.
[13] R.C. Atwood, P.D. Lee, J. Mater. Sci. 39 (2004) 7193–7197.
[14] D. M. Xu, Research Report of National Defense of Harbin Institute of Technology, vol. 12, 2000, 1–76.
[15] E. Koleva, K. Vutova, G. Mladenov, Vacuum 62 (2001) 189–196.